Journal of Zhejiang University-SCIENCE A (Applied Physics & Engineering)
ISSN 1673-565X (Print); ISSN 1862-1775 (Online)
www.jzus.zju.edu.cn; www.springerlink.com
E-mail: jzus@zju.edu.cn

Mass transfer enhancement of hollow fiber membrane deoxygenation by Dean vortices*#

Qing-ran KONG, Yi-zhen ZHANG, Hua TIAN, Li-feng FANG,
Ming-yong ZHOU, Li-ping ZHU, Bao-ku ZHU†‡

Key Laboratory of Macromolecule Synthesis and Functionalization (Ministry of Education), Key Laboratory of Adsorption and Separation Materials & Technologies of Zhejiang Province, ERC of Membrane and Water Treatment (Ministry of Education), Department of Polymer Science and Engineering, Zhejiang University, Hangzhou 310027, China

†E-mail: zhubk@zju.edu.cn

Received May 7, 2019; Revision accepted July 5, 2019; Crosschecked July 16, 2019

Abstract: This paper reports a modeling and experimental study of the mass transfer enhancement of water deoxygenation by using a helical hollow fiber membrane (HHFM) to enable Dean vortices. Experiments demonstrated that the HHFM deoxygenating rate was doubled compared with straight hollow fiber deoxygenation. A new model to describe the HHFM deoxygenation mass transfer was derived combining the helical coordinate system mass continuity equation on the lumen side and a modified dusty gas model for the mutual gaseous diffusion in the porous membrane. The model simulation showed that Dean vortices induce transverse fluid disturbance in the fiber, which significantly promotes lumen side mass transfer. The key parameters influencing the strength of Dean vortices are the Reynolds number of the lumen side and the curvature of HHFM. Operating and membrane structure parameters were optimized for HHFM deoxygenation design. The new model could be employed to describe quantitatively the mass transfer behavior of all types of HHFM gas-phase separation processes.

Key words: Mass transfer; Hollow fiber membrane; Water deoxygenation; Dean vortices
https://doi.org/10.1631/jzus.A1900181 **CLC number:** TQ021.4

1 Introduction

Hollow fiber membrane processes have been widely applied to membrane degassing (Sethunga et al., 2018), gas absorption (Henares et al., 2018), ultrafiltration (Wu CR et al., 2018), membrane extraction (Ferreira et al., 2015), etc. Evidence (Henares et al., 2018) has shown that lumen side mass transfer limitation, which is due to the non-optimized laminar flow pattern, restricts the performance of the membrane module and thus improvement in the liquid flowing condition on the lumen side is a key factor in the optimal design of the process. Among the available methods, the use of helical hollow fiber membrane (HHFM) is effective by inducing a secondary flow in the hollow fibers (Fig. 1a), and it significantly improves the lumen side mass transfer rate (Al-Bastaki and Abbas, 2001). The secondary flow, namely, Dean vortices, occurs when the fluid flows in the HHFM in a spiral path. In the HHFM, there always exists a transverse pressure gradient on the cross-section of the fiber, which supplies a centripetal force for altering the fluid direction. The pressure gradient needed for the faster-flowing center fluid is, however, larger than that needed for the slower flowing fluid near the fiber wall. This leads

‡ Corresponding author
* Project supported by the National Key R&D Program of China (No. 2017YFE0114100), and the National High-Tech R&D Program (863 Program) of China (No. 2012AA03A602)
# Electronic supplementary materials: The online version of this article (https://doi.org/10.1631/jzus.A1900181) contains supplementary materials, which are available to authorized users
ORCID: Qing-ran KONG, https://orcid.org/0000-0002-0749-9161; Bao-ku ZHU, https://orcid.org/0000-0002-3221-181X

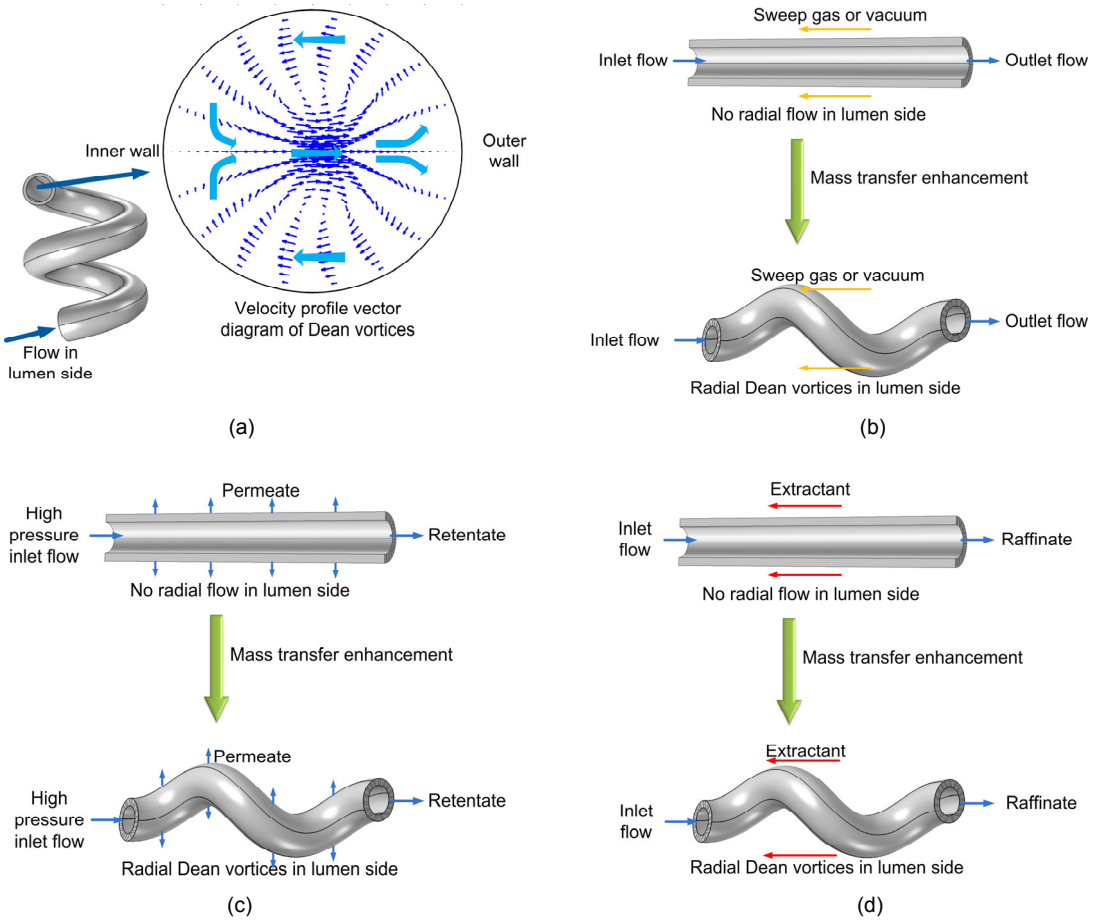

Fig. 1 Schematic diagrams of Dean vortices in HHFM (a), mass transfer enhancement of membrane gas transfer process (b), membrane ultrafiltration (c), and membrane extraction (d)

to the central area fluid in the fiber flowing towards the outside wall and the fluid near the wall flowing inwards, which forces the lumen side fluid to form two vortices on the cross-section. These two vortices will directly carry the lumen side solute from the central area to the wall and subsequently enhance the mass transfer rate. Since the velocity profiles of a helical tube were first investigated by Dean (1927), the perturbation and numerical solutions to the Dean vortices have been much studied. A more detailed introduction to Dean vortices can be found in (Zhou and Shah, 2004). Previous progress on describing the velocity profile of HHFM provides a clear image of Dean vortices, which is also fundamental for further research in HHFM mass transport.

Experimental evidence of mass transfer enhancement with HHFM has been reported in gas absorption (Kaufhold et al., 2012), ultrafiltration (Moll et al., 2007), and membrane extraction (Liu et al., 2005) (Figs. 1b–1d). The results indicate HHFMs can promote the lumen side mass transfer rate 2–4 times compared with a straight hollow fiber. Nevertheless, little has been published on the mathematical modeling of these processes, which is probably due to the complexity of mass transfer in a helical fiber and a porous membrane. Jani et al. (2011) and Mejia Mendez et al. (2017) simulated the mass transfer of oxygen and CO_2 absorption in HHFM in the Cartesian coordinate system with a numerical solution velocity profile. Simulation of these cases only involves the dissolved gas mass transfer profile in the lumen side; the mutual gaseous components mass transfer in the porous membrane has not been considered. For the cases of water deoxygenation and a blood oxygenator with HHFM, however, mutual gaseous diffusion of O_2, N_2, H_2O, etc. exists in the porous membrane (Shao et al., 2008; Turri and Yanagihara, 2011), so the mass transfer of the lumen side and mutual gaseous

diffusion in the porous membrane must simultaneously be taken into account. Besides, simulation with a numerical solution velocity profile and a Cartesian coordinate system continuity equation of HHFM in these two operations can be time-consuming. Other literature concerning computational fluid dynamics (CFD) simulation of HHFM process only gives the numerical profile of the velocity without solving the mass transfer equations (Motevalian et al., 2016). To understand the mass transfer mechanism and select optimal operating parameters of water deoxygenation and blood oxygenator, modeling and simulation are still needed.

This work concentrates on the mass transfer modeling of the mutual gas-transfer helical hollow fiber process. Our specific interest is in vacuum water deoxygenation. In our previous paper (Kong et al., 2017), a mass continuity equation was derived to describe the mass transport of membrane extraction in HHFM. A perturbation solution (Zhang and Zhang, 2000) of Dean vortices was used to describe the velocity profile in the lumen side. This model can also describe the HHFM mass transfer of dissolved gases of the lumen side for this work. The gaseous mutual-component mass transfer in the porous membrane, on the other hand, is usually considered as a Poiseuille-Knudsen transition mechanism, which is described by the well-known dusty gas model (Hitsov et al., 2015). To accelerate the computational efficiency of the dusty gas model, a modified version of the model with the Fick-diffusion formed equations suggested by Kong et al. (2012) was employed. In the present paper a new model to describe the vacuum water deoxygenation with Dean vortices is first derived. Concentration profiles of oxygen, nitrogen, and water in the lumen and the membrane are calculated to investigate the mass transfer mechanism of HHFM deoxygenation. Experiments are then conducted to demonstrate the performance of HHFM on water deoxygenation. The influences of aqueous velocity, vacuum degree, and temperature on the HHFM deoxygenation efficiency are tested. The long term stability of HHFM deoxygenation is evaluated. Computational results are compared with both experiment and data from the literature to verify the accuracy of the simulation. Finally, the influences of key operating parameters are investigated by simulation, and optimized membrane and operating parameters are selected.

2 Modeling

2.1 Mass transfer equations

A membrane module usually contains many hollow fiber membranes with identical mass transport behavior, and therefore only one hollow fiber membrane is modeled in this work to represent the overall performance. The dissolved gases mass transfer of the hollow fiber membrane degassing can generally be divided into three steps as shown in Fig. 1b. Firstly, the dissolved gases, i.e. O_2, N_2, CO_2, and noble gases, transfer from the lumen side bulk aqueous flow to the membrane wall. This process is driven by both diffusion (the radial concentration gradient) and convection (Dean vortices). Secondly, the dissolved gases gasify at the aqueous-membrane interface and diffuse through the porous membrane to the shell side. Finally, the shell side gaseous mixture is drawn out of the membrane module by vacuuming the shell side. The mass transfer behavior can be described by the steady state mass continuity equation (Li et al., 2018) in Eq. (1) and the heat transfer is negligible.

$$\nabla\left(-D_i\nabla c_i\right)+\nabla \boldsymbol{v}c_i=0, \tag{1}$$

where D is the diffusivity; c is the concentration; $\boldsymbol{v}$ is the velocity profile; the subscript i stands for property of the ith component.

The lumen side mass transfer equation (Kong et al., 2017) of the HHFM in Eq. (2) was derived from the mass continuity equation in a 3D orthogonal helix coordinate system:

$$\begin{aligned} &v_r\frac{\partial c_i}{\partial r}+\frac{v_\theta}{r}\frac{\partial c_i}{\partial \theta}+\frac{v_z}{1+\kappa r\cos\theta}\frac{\partial c_i}{\partial z}\\ &\qquad=D_i\frac{\partial^2 c_i}{\partial r^2}+\frac{D_i}{r^2}\frac{\partial^2 c_i}{\partial \theta^2}+\frac{D_i}{r}\frac{\partial c_i}{\partial r},\\ &\kappa=r_c\Big/\left(r_c^2+\left(p_c/(2\pi)\right)^2\right), \end{aligned} \tag{2}$$

where κ is the curvature of HHFM; r_c is the curvature radius of HHFM; p_c is the pitch of HHFM; r, θ, and z are the radial, azimuth, and axial directions of the cylindrical coordinate system, respectively.

The first two terms $v_r\frac{\partial c_i}{\partial r}+\frac{v_\theta}{r}\frac{\partial c_i}{\partial \theta}$ on the left side of Eq. (2) indicate the contribution of the Dean

vortices to the mass transfer by convection. The secondary term $\frac{D_i}{r^2}\frac{\partial^2 c_i}{\partial\theta^2}$ of the right side illustrates diffusion in the tangential direction. More details of the derivation of Eq. (2) can be found in our previous work (Kong et al., 2017). The velocity profiles v_r and v_θ of the Dean vortices can be expressed by a third-order perturbation solution (Zhang and Zhang, 2000). Simulation indicated that the second- and third-order terms show a negligible effect on the velocity (less than 0.8%), and therefore only the zero- and first-order terms were adopted in Eqs. (3)–(5).

$$v_r=\left[-Re^2\kappa r_1\left(r^{*2}-1\right)^2\left(r^{*2}-4\right)\cos\theta\right]\Big/288, \tag{3}$$

$$v_\theta=\left[Re^2\kappa r_1\left(7r^{*6}-30r^{*4}+27r^{*2}-4\right)\sin\theta\right]\Big/288, \tag{4}$$

$$\begin{aligned}v_z=&Re\left(1-r^{*2}\right)+\frac{\kappa r_1 Re^3\cos\theta}{11520}\left(r^*-r^{*3}\right)\\&\times\left(8640/Re^2-19+21r^{*2}-9r^{*4}+r^{*6}\right),\end{aligned} \tag{5}$$

where Re is the Reynolds number of lumen side; r_1 is the inner radius of the hollow fiber membrane, and $r^*=r/r_1$ is the dimensionless radius.

The velocity profile of the lumen side is considered to be fully developed because the transition distance to form the Dean vortices in HHFM is relatively short (less than 3% of the total length of hollow fiber) as estimated in (Austin and Seader, 1974). Note that the mass transfer of CO_2 and noble gases in the lumen side does not affect the mass transfer of O_2, which is the main component considered in this work, so their mass transfer was not modeled and simulated.

The mass transfer behavior of O_2, N_2, CO_2, noble gases, and water vapor in the porous membrane is determined by the relationship between the gaseous molecular mean free path of each component and the average membrane pore diameter, which can be evaluated by the Knudsen number (Lee et al., 2018) in Eq. (6).

$$k_n=\frac{\lambda}{2r_1}=\frac{k_B T}{2\sqrt{2}\pi\sigma^2 p r_1}, \tag{6}$$

where k_n is the Knudsen number, and $k_n\geq1$ is the Knudsen diffusion mechanism, $0.01<k_n<1$ is the Poiseuille-Knudsen transition mechanism, $k_n\leq0.01$ is the Poiseuille mechanism; λ is the mean free path of gas; k_B is the Boltzmann constant; T is the temperature; σ is the gas collision diameter; p is the pressure.

An estimate of the Knudsen number is from 0.10–0.80 based on the experimental and simulation parameters of this work, indicating a Poiseuille-Knudsen transition mechanism. So the well-known dusty gas model (Servi et al., 2017) with the Darcy law (Wu DZ et al., 2018) and gas mixture viscosity (Wilke, 1950) in Eqs. (7)–(10) could be employed to describe the gaseous multi-component transport in the membrane pores.

$$\begin{aligned}\boldsymbol{N}_i=\boldsymbol{J}_i+c_i\boldsymbol{v}^{\mathrm{m}}=&\left(-\nabla c_i+\sum_{j\neq i}\frac{\boldsymbol{J}_j x_i}{\tilde{D}_{ij}}-\frac{c_i\boldsymbol{v}^{\mathrm{m}}}{D_{i\mathrm{k}}}\right)\\&\Big/\left(\sum_{j\neq i}\frac{x_j}{\tilde{D}_{ij}}+\frac{1}{D_{i\mathrm{k}}}\right)+c_i\boldsymbol{v}^{\mathrm{m}},\end{aligned} \tag{7}$$

$$\boldsymbol{v}=-\frac{B}{\mu_{\mathrm{mix}}}\nabla p=-\frac{B}{\mu_{\mathrm{mix}}}\sum\nabla c_i RT, \tag{8}$$

$$B=\frac{\varepsilon}{\tau}\frac{d_p^2}{32}, \tag{9}$$

$$\mu_{\mathrm{mix}}=\sum_{i=1}^{n}\left(x_i\mu_i\Big/\sum_{j=1}^{n}x_j\phi_{ij}\right), \tag{10a}$$

$$\phi_{ij}=\frac{\left[1+\left(\mu_i/\mu_j\right)^{1/2}\left(M_j/M_i\right)^{1/4}\right]^2}{\left[8\left(1+\left(M_i/M_j\right)\right)\right]^{1/2}}, \tag{10b}$$

where $\boldsymbol{N}$ is the combined molecular flux; $\boldsymbol{J}$ is the molecular diffusion flux; x is the mole fraction; $\tilde{D}$ is the Maxwell–Stefan diffusivity; $D_{i\mathrm{k}}$ is the Knudsen diffusivity; $\boldsymbol{v}^{\mathrm{m}}$ is the molar average velocity; B is the permeability of Darcy law; R is the gas constant; μ is the viscosity; ε is the membrane porosity; τ is the tortuosity; d_p is the diameter of membrane pore; ϕ is the parameter of gas mixture viscosity equation; M is the molecular weight; the subscript mix is the property of mixture.

These equations show strong interaction of the gaseous mutual components on the mutual diffusion, so that O_2, N_2, and water, which all have significant partial pressures in the porous membrane, must be modeled and simulated simultaneously. The CO_2 and noble gases, on the other hand, are expected to have small partial pressures of less than 1% in the gaseous

mixture, which is estimated according to the gas component of the dry air (NIST, 2018), so they can be ignored in modeling of the gas phase without introducing a significant error. The numerical simulation process of the three-component dusty gas model with O_2, N_2, and H_2O, remains, however, quite complex and time-consuming, so a modified dusty gas model equation in Eqs. (11)–(14) suggested by Kong et al. (2012) was adopted in this work.

$$\boldsymbol{N}_i = -D_i^* \nabla c_i + c_i \boldsymbol{v}_i^*, \tag{11}$$

$$\begin{aligned} D_i^* = &\left\{ D_{ik} \varepsilon / \tau \left[\left(1-x_i\right) / \sum\nolimits_{j\neq i} \left(x_j / D_{ij} \right) \right] \right\} \\ &\Big/ \left\{ \left(1-x_i\right) / \sum\nolimits_{j\neq i} \left(x_j / D_{ij} \right) \right. \\ &\left. + x_i \left[\left(1-x_i\right) / \sum\nolimits_{j\neq i} \left(x_j / D_{jk} \right) \right] + D_{ik} \left(1-x_i\right) \right\}, \end{aligned} \tag{12}$$

$$\begin{aligned} \boldsymbol{v}_i^* = &-\frac{B}{\mu_{\mathrm{mix}}} \nabla p \\ &- \left\{ D_{ik} \nabla p / p \left[\left(1-x_i\right) / \sum\nolimits_{j\neq l} \left(x_j / D_{jk} \right) \right] \right\} \\ &\Big/ \left\{ \left(1-x_i\right) / \sum\nolimits_{j\neq l} \left(x_j / D_{lj} \right) \right. \\ &\left. + x_i \left[\left(1-x_i\right) / \sum\nolimits_{j\neq l} \left(x_j / D_{jk} \right) \right] + D_{ik} \left(1-x_i\right) \right\}, \end{aligned} \tag{13}$$

$$\frac{\partial \left(-D_i^* \nabla c_i + c_i \boldsymbol{v}_i^* \right)}{\partial r} + \frac{1}{r} \left(-D_i^* \nabla c_i + c_i \boldsymbol{v}_i^* \right) = 0, \tag{14}$$

where the superscript $*$ stands for variables of the modified dusty gas model.

Kong et al. (2012) commented that the Fick-diffusion formed equation gives a much faster calculation speed and yet acceptable accuracy. Boundary conditions (Tan et al., 2005) of the model equations are listed below.

Lumen side aqueous phase:

$$z = 0: \quad c_i = c_{i,\mathrm{f}}, \tag{15}$$

$$z = l: \quad \left(\partial c_i / \partial z \right) = 0, \tag{16}$$

$$r = 0: \quad \left(\partial c_i / \partial r \right) = 0. \tag{17}$$

Lumen side-membrane pores interface:

$$\begin{aligned} r = r_1: \quad & \left(D_i \partial c_i / \partial r \right) \Big|_{\mathrm{lumen}} = \boldsymbol{N}_i \Big|_{\mathrm{membrane}} \\ & = \left(-\bar{D}_i \nabla c_i + c_i \bar{\boldsymbol{v}} \right) \Big|_{\mathrm{membrane}}, \end{aligned} \tag{18}$$

$$r = r_1: \quad H_i c_i / \left[RT \left(c_i + \rho_{\mathrm{w}} / M_{\mathrm{w}} \right) \right] \Big|_{\mathrm{lumen}} = c_i \big|_{\mathrm{membrane}}, \tag{19}$$

$$r = r_1: \quad c_{\mathrm{H_2O}} \Big|_{\mathrm{membrane}} = p_{\mathrm{w}}. \tag{20}$$

Membrane pores-shell side interface:

$$r = r_2: \quad \left(RT \sum c_i \right) \Big|_{\mathrm{membrane}} = p \big|_{\mathrm{shell}}, \tag{21}$$

$$r = r_2: \quad \left(c_i / \sum c_i \right) = N_i / \sum N_i, \tag{22}$$

where l is the length of hollow fiber; ρ is the density; H is Henry's law solubility constant; r_2 is the outer radius of the hollow fiber membrane; the subscripts f and w are the feed solution and water, respectively.

Note that the simulation of mass transfer in the porous membrane was conducted for O_2, N_2, and H_2O simultaneously. The boundary condition equation (Eq. (21)) shows an overall mass conservation of O_2, N_2, and H_2O along the membrane-shell side interface, so the summation of the concentrations of these three gases at any point of the membrane-shell side interface is identical. The porous membrane is considered as non-wetting due to the hydrophobic nature of the polypropylene membrane.

2.2 Model parameters and simulation process

The diffusivities in aqueous phase (Wilke and Chang, 1955), gaseous phase (Fuller et al., 1966), and Knudsen diffusivity (Solsvik and Jakobsen, 2011) were estimated by empirical correlations in Eqs. (23)–(25).

$$D_i = \frac{7.4 \times 10^{-8} \left(\alpha M_i \right)^{0.5} T}{\mu_{\mathrm{w}} V_i^{0.6}}, \tag{23}$$

$$D_{ij} = \frac{3.204 \times 10^{-8} T^{1.75} (1/M_i + 1/M_j)^{0.5}}{p (v_i^{1/3} + v_j^{1/3})^2}, \tag{24}$$

$$D_{ik} = \frac{d_{\mathrm{p}}}{3} \left(\frac{8RT}{\pi M_i} \right)^{0.5}, \tag{25}$$

where α is the association parameter; V is the molal volume of solute at normal boiling point.

The viscosities, saturated water vapor pressure and Henry law's coefficients of O_2, N_2, and H_2O were obtained from the NIST website (NIST, 2018). All the

parameters used in simulations from 278.2 to 308.2 K are shown in Table S1.

The model equations with the boundary conditions (Eqs. (2)–(5) and (11)–(22)) were solved numerically by COMSOL version 4.0. The size of the z direction was narrowed to 1/800 to eliminate the large mismatch in size of the r and z directions. The straight hollow fiber membrane (SHFM) deoxygenation cases were simulated with κ=0 for comparison with the HHFM ones. The grid independence analysis indicates that the number of cells larger than 150 000 could lead to a relative deviation of C_{out} (Eq. (26)) of less than 0.05%, so 150000 cells were employed in the simulation. Note that the mass continuity equation was solved for O_2 and N_2 in the lumen side, while for O_2, N_2, and H_2O for the porous membrane.

Two indicators were defined to evaluate the membrane degassing performance. The lumen side outlet dimensionless O_2 concentration C_{out} is calculated by

$$C_{out}=\iint_S v_z\, c\big|_{z=l}\,\mathrm{d}\sigma \Big/ \left(c_f \iint_S v_z \mathrm{d}\sigma\right), \tag{26}$$

where v_z, c_f, and S refer to the z-direction velocity distribution of lumen, lumen side inlet O_2 concentration, and the fiber cross section area.

The enhancement factor E is used to indicate mass transfer enhancement of HHFM deoxygenation results compared with SHFM ones under the same operating conditions as follows:

$$E=\left(1-C_{out}\right)_{HHFM}/\left(1-C_{out}\right)_{SHFM}. \tag{27}$$

3 Experimental

The experimental setup of HHFM deoxygenation is shown in Fig. 2a. The membrane modules for the hollow fiber membrane deoxygenation experiment were filled with HHFM bundles (#1) and SHFMs (#2) with identical effective length. The HHFM bundle was obtained by twisting three straight polypropylene fibers with each other, forming uniform pitch and curvature diameter (Fig. 2b). Details of the module parameters are listed in Table 1. Deionized water was used as the oxygen-enriched water for degassing tests from a 10 L water tank. The water tank had been blown with fresh air for more than 6 h at a set temperature before the experiment so as to

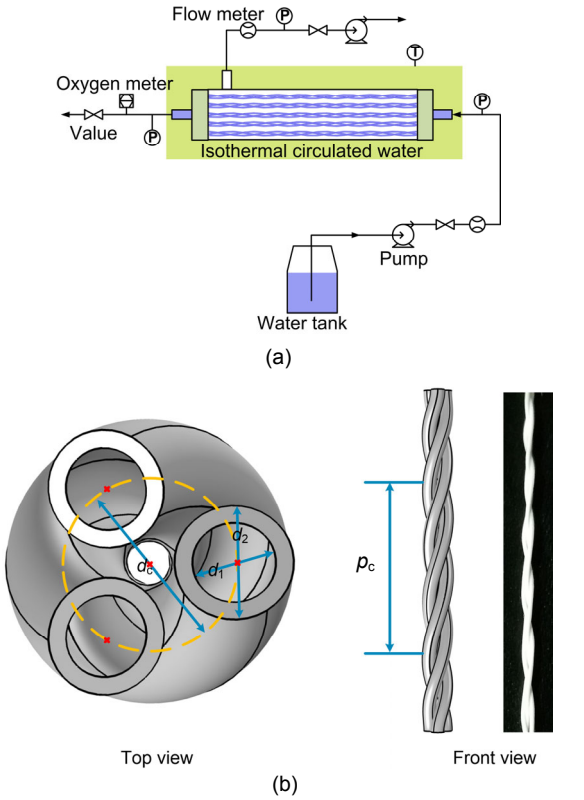

Fig. 2 Experimental setup of HHFM deoxygenation experiments (a), and structural parameters of a helical fiber bundle (three straight hollow fiber membranes twisted together) (b)

d_1, d_2, d_c, and p_c stand for fiber inner diameter, fiber outer diameter, curvature diameter, and pitch, respectively

Table 1 Parameters of the hollow fiber membrane and contactors

Item	Description
Curvature diameter, d_c (mm)	1.0±0.1 (#1 Helical); – (#2 Straight)
Effective hollow fiber length, l (m)	0.4
Fiber inner diameter, d_1 (μm)	400±20
Fiber outer diameter, d_2 (μm)	500±20
Length of module (m)	0.50
Maximum diameter of pores (nm)	200
Membrane porosity, ε	0.45
Membrane tortuosity, τ	2.2
Module inner diameter (mm)	18
Number of fibers	120
Packing density	~0.10
Pitch, p_c (mm)	15±2 (#1 Helical); – (#2 Straight)

saturate it with dissolved air. The water phase was pumped through the lumen side of the membrane module in a single pass while the shell side was kept at a known vacuum degree by a vacuum pump. The dissolved oxygen concentrations of both inlet and outlet of the lumen side were monitored by on-line dissolved oxygen meters (MIK-D06000, Hangzhou Asmik Sensing Technology Co., Ltd., China). The temperature of each degassing experiment was fixed at a known value by putting the whole experimental apparatus in a thermostatic water-bath.

The mean velocity of the lumen side $\overline{v}$, the dimensionless absolute pressure of the shell side p/p_0, and the temperature T, were verified during the experiments to investigate their influences on deoxygenation tests. The ranges of these operating parameters cover the applicable range of the commercial membrane module. Experiments were performed for both #1 and #2 with identical operating parameters for comparison. Three parallel experiments were carried out for each experimental run to eliminate random error with an average value taken as the result. A long term run of HHFM deoxygenation was implemented under a typical operating condition of T=298.2 K, $\overline{v}$ =0.1 m/s, and p/p_0=0.50 for 100 h. The experimental errors were estimated and are listed in Table 2.

Table 2 Uncertainty estimation of experimental sensors and obtained parameters

Variable	Typical range	Uncertainty
Experimental sensors		
Dissolved oxygen tester (g/m^3)	0–20	±1% of full scale
Flow rate (L/min)	0–1.2	±1% of full scale
Pressure (kPa)	0–300	±1% of full scale
Temperature (K)	278.2–308.2	±1% of full scale
Obtained parameters		
Dissolved oxygen concentration (g/m^3)	0–20	2.3%
Curvature (m^{-1})	0–200	2.1%
Mean velocity (m/s)	0–1.5	1.5%

4 Results and discussion

4.1 Experimental results

Values of dependent and independent variables are summarized in Table S2. Fig. 3 depicts the variation of the lumen side outlet O_2 concentration and the enhancement factor with different lumen side Reynolds number and shell side vacuum degree (represented by absolute pressure). C_{out} shows an increase with a rise in the lumen side Reynolds number, however, it decreases with the shell side absolute pressure over the range of operating conditions in Figs. 3a and 3b. For both HHFM and SHFM, a higher lumen side Reynolds number leads to a shorter mass transfer contact time and, subsequently, a lower mass transfer rate and a higher C_{out}. A lower shell side absolute pressure, on the other hand, reduces the partial pressures of O_2 and N_2 on the lumen side-membrane interface, resulting in a higher radial concentration gradient of the lumen side and a faster radial mass transfer rate. Fig. 3c illustrates a clear trend in the effect of the Dean vortices on membrane degassing by estimating the enhancement factor. The enhancement factor increases with the Reynolds number of the lumen side, reaching about 2.5 at Re=544. This suggests that the HHFM is more favorable when applied to membrane processes with a high liquid velocity in the lumen side. The shell side vacuum degree, however, shows a negligible effect on the enhancement factor. This may be understood by Eqs. (2)–(5) showing that the intensity of Dean vortices is decided only by the Reynolds number and the curvature of the HHFM.

Fig. 4 depicts the influence of temperature on the lumen side outlet O_2 concentration and the enhancement factor. Figs. 4a and 4b indicate that a high temperature is favorable for degassing. A higher temperature leads to higher diffusivities of both aqueous and gas phase and lower equilibrium partial pressures of dissolved gases. These two factors simultaneously facilitate the mass transfer of the dissolved gases. Therefore, the transverse convection of HHFM promotes mass transfer more significantly at a lower temperature, where the mass transfer resistance of lumen side diffusion is more predominant, as shown in Fig. 4c.

The trans-membrane pressures were measured by the pressure difference between the inlet pressure of the lumen side and the absolute pressure of the shell side and, to keep the operation safe, should be lower than the breakthrough pressure. We set the absolute pressure of the vacuum side to its minimum value (about 5 kPa) to get the maximum pressure difference Δp_{max} when we measured the

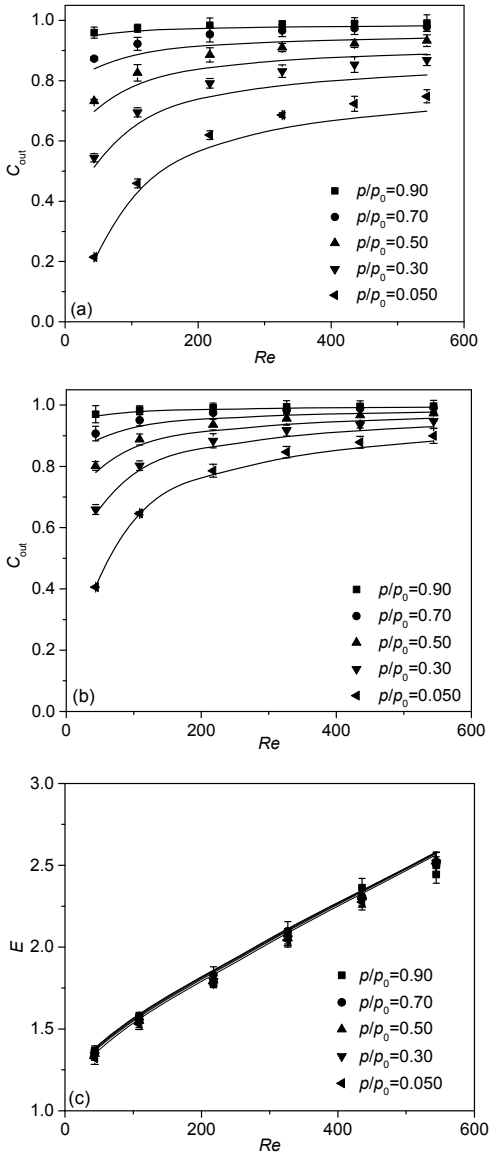

Fig. 3 Effect of lumen side Reynolds number and gas phase absolute pressure of the shell side on the aqueous phase outlet O_2 concentration in (a) HHFM deoxygenation (#1, κ=162.9 m^{-1}), (b) SHFM deoxygenation (#2, κ=0), and (c) the enhancement factor at T=298.2 K. The standard deviations were calculated from three parallel experimental data

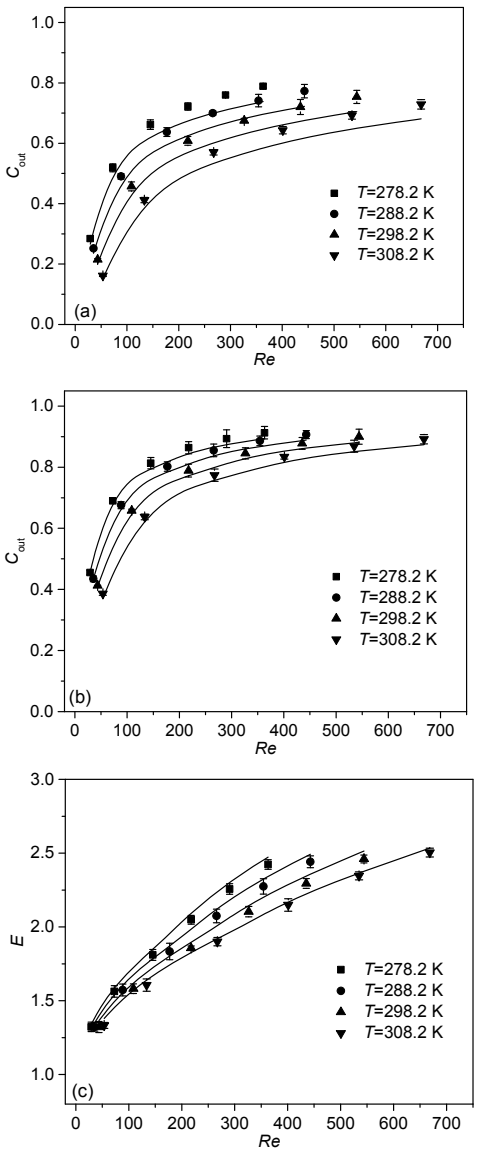

Fig. 4 Effect of temperature and lumen side Reynolds number on the aqueous phase outlet O_2 concentration in (a) HHFM deoxygenation (#1, κ=162.9 m^{-1}), (b) SHFM deoxygenation (#2, κ=0), and (c) the enhancement factor at p/p_0=0.050. The standard deviations were calculated from three parallel experimental data

trans-membrane pressure in Fig. 5. The maximum trans-membrane pressure in all experiments is lower than 230 kPa, lower than the breakthrough pressure of 500 kPa estimated by Kong et al. (2016), indicating that the HHFM and SHFM deoxygenation operation is safe within the experimental operating range. The HHFM experiments show a higher trans-membrane pressure than SHFM under the same operating conditions, which indicates the HHFM process requires extra energy to form a transverse flow disturbance in the lumen side. The long term test contained a 100 h run for HHFM deoxygenation, and showed an unchanged performance of the membrane module as shown in Table S3.

The HHFM and SHFM deoxygenation experiments were also simulated by Eqs. (2)–(5) and (11)–(22) and are shown in Figs. 3 and 4, where good consistency between simulation curves and experimental points can be observed. The relative errors (Kong et al., 2013) of C_{out} are all lower than 7%. The accuracy of model equations was also testified by simulating data from Liu et al. (2005) and Kaufhold et al. (2012). The boundary conditions used in these two cases are listed in Table S4, and the simulation results are shown in Fig. 6. The mean relative error between the experimental and simulation results is 12%, indicating good simulation accuracy.

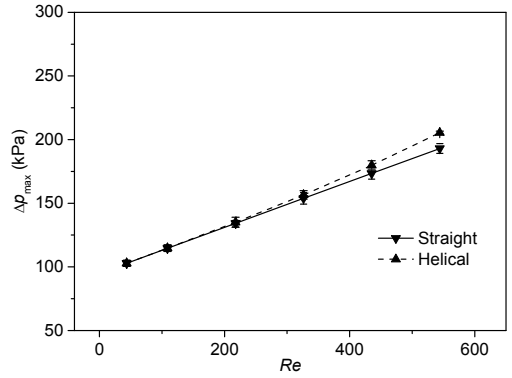

Fig. 5 Maximum trans-membrane pressure difference of the helical (#1, κ=162.9 m^{-1}) and straight (#2, κ=0) hollow fiber contactors with variation of lumen side Reynolds number at T=298.2 K, p/p_0=0.05. The standard deviations were calculated from three parallel experimental data

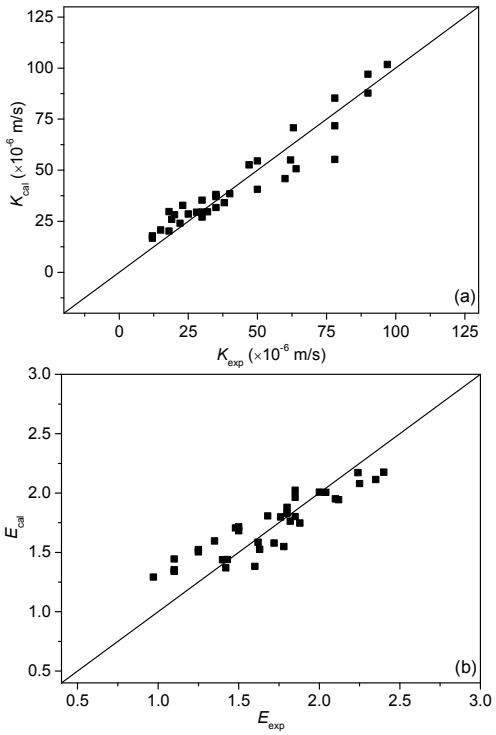

Fig. 6 Comparisons between simulation results with experimental data from Figs. 1–3 of Liu et al. (2005) (a) and Figs. 1–3 of Kaufhold et al. (2012) (b)

4.2 Concentration profiles

Figs. 7a and 7b illustrate the cross-section concentration profiles for O_2 of HHFM and SHFM deoxygenation, and exhibit a clear picture of the influence of Dean vortices on mass transfer. Fig. 7a shows that the highest O_2 concentration areas on the lumen side coincide precisely with the vortices (Fig. 1a), exhibiting two symmetric ovals. In those areas, the convective mass transfer generated by the turbulent flow has almost vanished and, therefore, only diffusion drives the mass transport. Outside the vortex center areas, however, the Dean vortices circulate O_2 from the lumen center to the outer wall, and then turn back along the wall to the inner wall through two convective channels. These convective channels significantly promote the lumen side mass transfer, and similarly decrease the mass transfer resistance by the lumen-membrane interface. Compared with SHFM deoxygenation in Fig. 7b, where no transverse velocity exists, the concentration profile of HHFM deoxygenation vividly illustrates the mass transfer enhancement mechanism of Dean vortices.

Figs. 7c and 7d show the axial direction concentration profiles of O_2 for HHFM and SHFM deoxygenation. Two high concentration areas due to the influence of Dean vortices along the axial direction can be seen. The maximum concentration gradient exists near the boundary r=r_1, which indicates that mass transfer resistance of O_2 within the lumen side is still dominant, although Dean vortices have significantly promoted mass transfer. There exists a jump of O_2 concentration along the lumen-membrane boundary due to a high value of Henry's coefficient. The O_2 concentration in the membrane exhibits a slight decrease along the r-direction, indicating that membrane mass transfer resistance is unobvious in this case. The concentration profiles of N_2 and H_2O were obtained simultaneously in the simulation and are shown in Figs. S1 and S2, where similar concentration profiles as the O_2 ones can be found.

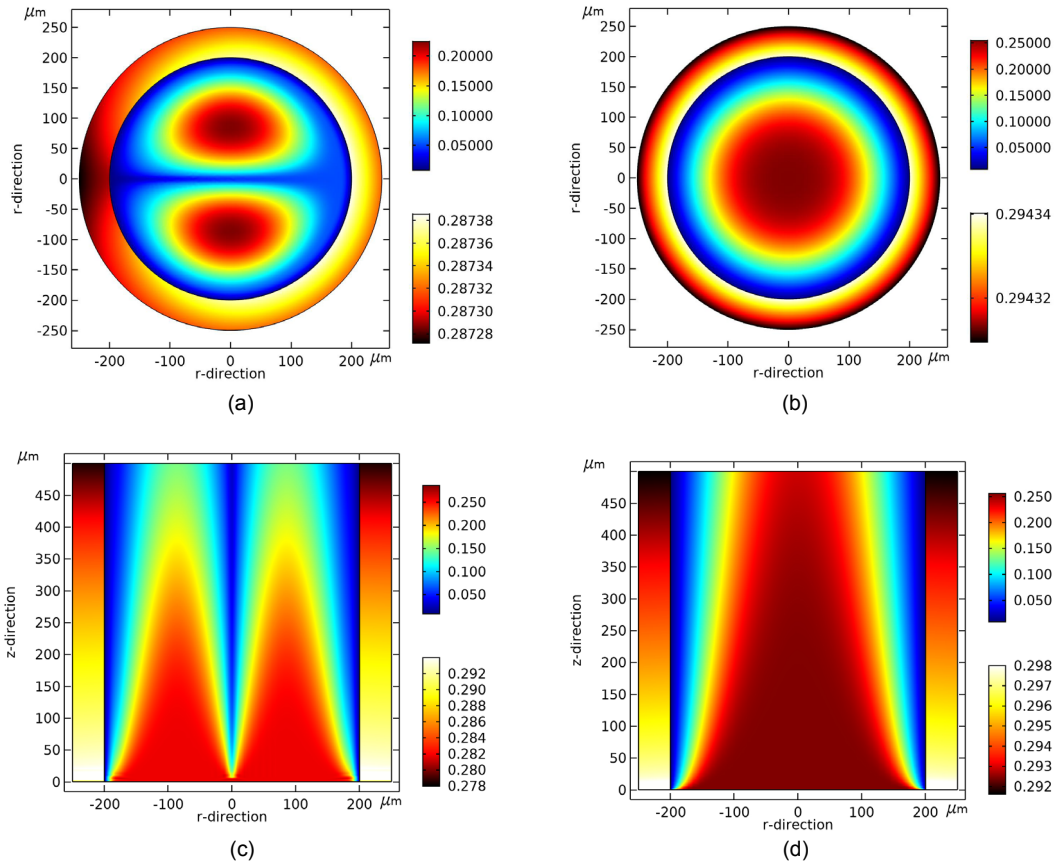

Fig. 7 Concentration profiles of O_2 of HHFM deoxygenation (κ=162.9 m^{-1}, C_{out}=0.319, z=0.5 m) (a) and SHFM deoxygenation (κ=0, C_{out}=0.586, z=0.5 m) (b) on the cross-section, and HHFM deoxygenation (κ=162.9 m^{-1}, C_{out}=0.319) (c) and SHFM deoxygenation (κ=0, C_{out}=0.586) (d) along the axis direction. Re=217, T=298.2 K, $\bar{v}$ =0.5 m/s, p/p_0=0.50, and l=1.0 m

4.3 Effects of curvature

According to Eqs. (2)–(5), Re and κ are key factors affecting the intensity of the radial flow disturbance. In this section, simulation was conducted to study the influences of Re and κ on the lumen side O_2 concentration C_{out} and the enhancement factor E. Fig. 8a shows that C_{out} decreases with an increase of κ and a decrease of Re. However, a remarkable effect of both the parameters is located in the large Re and small κ region, and shows that, when the diffusion mass transfer is limited at a high velocity, a small κ will lead to a pronounced enhancement of degassing. As Re increases, however, the influence of κ becomes inconspicuous, and a larger κ is needless. To illustrate the effect of Re and κ on E more clearly, Fig. 8b shows the trend of the enhancement factor E with Re and κ. Fig. 8b shows that a significant promotion of E exists on the region of a large Re and small κ. The mass transfer efficiency is improved 1.8–2.2 times from SHFM deoxygenation to HHFM with an identical Re. For insufficient degassing at a large Re, the Dean vortices exhibit a remarkable influence on promoting mass transfer performance, while for sufficient degassing at a small Re, the influence tends to be attenuated. Figs. 8a and 8b indicate that Dean vortices show high efficiency on mass transfer only at the entrance area of HHFM.

Fig. 9 depicts a design drawing to optimize the Re and κ at a certain C_{out}. The steep changes of lines of Fig. 9 illustrate that, for a laminar flow pattern, even a small value of κ ($0<\kappa<50$ m^{-1}) will lead to a doubled E. For a given C_{out} concentration, any HHFM configuration proves that a curvature smaller than 50 m^{-1} would be expected significantly to promote the degassing performance, which indicates that twisted, coiled, and meander shaped (Kaufhold et al., 2012) hollow fiber membranes are all suitable. For

example, with C_{out}=0.050 and κ=50 m^{-1}, *Re* should be 46.2 from Fig. 9. The optimized parameters are $\bar{v}$ =0.11 m/s, r_1=200 μm, r_c=10 mm, p_c=63 mm, p/p_0=0.050, T=298.2 K, and l=1.0 m. Both simulation and experiment testify that using HHFM deoxygenation instead of SHFM will obtain a doubled mass transfer rate.

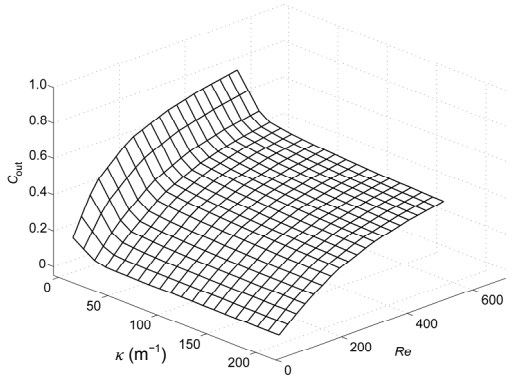

(a)

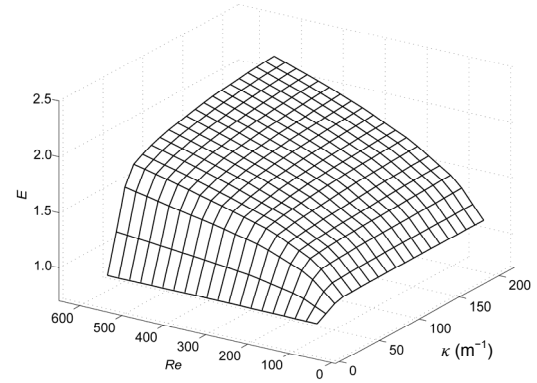

(b)

Fig. 8 Effect of curvature and lumen side Reynolds number on the aqueous phase outlet O_2 dimensionless concentration of the lumen side (a) and enhancement factor (b). T=298.2 K, p/p_0=0.050, and l=1.0 m

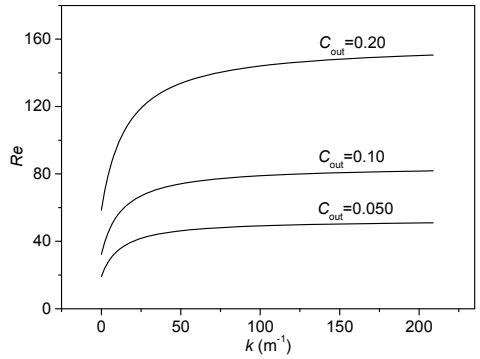

Fig. 9 Variation of lumen side Reynolds number with curvature at different C_{out}. T=298.2 K, p/p_0=0.050, and l=1.0 m

5 Conclusions

Both experiment and simulation demonstrated that the use of HHFMs in place of SHFMs is the simplest and most effective way to promote mass transfer in membrane deoxygenation. HHFM deoxygenation experiments showed doubled degassing efficiency compared with SHFM. Model simulation illustrated that Dean vortices generate transverse disturbance of the fibers and subsequently enhance the lumen side mass transfer rate. The vortices exist symmetrically on the cross-section of HHFM, and they depend on *Re* and κ. They circulate the dissolved gases to the wall, which promotes lumen side mass transfer efficiency.

A mathematical model for describing the concentration profiles of dissolved gases on the lumen side and the porous membrane was derived. The simulation results for the mean velocity of the lumen side, the shell side vacuum degree, and the temperature and curvature of HHFM are all in accordance with experimental ones. The performance of HHFM deoxygenation is mainly determined by the lumen side Reynolds number and the curvature of HHFM. A notable *E* exists on the area of a large *Re* and small κ, which indicates that Dean vortices show effective influence only at the entrance of HHFM where an inadequate mass transfer restricts degassing. Operating and membrane parameters were optimized to HHFM deoxygenation design. The new model could be applicable for describing the mass transfer behavior of all types of HHFM gas-phase separation processes.

Contributors

Qing-ran KONG and Bao-ku ZHU wrote the first draft of the manuscript. Qing-ran KONG, Yi-zhen ZHANG, and Hua TIAN performed the experiments. Qing-ran KONG, Li-feng FANG, Ming-yong ZHOU, and Li-ping ZHU revised and edited the final version.

Conflict of interest

Qing-ran KONG, Yi-zhen ZHANG, Hua TIAN, Li-feng FANG, Ming-yong ZHOU, Li-ping ZHU, and Bao-ku ZHU declare that they have no conflict of interest.

References

Al-Bastaki N, Abbas A, 2001. Use of fluid instabilities to enhance membrane performance: a review. *Desalination*, 136(1-3):255-262.

https://doi.org/10.1016/S0011-9164(01)00188-6

Austin LR, Seader JD, 1974. Entry region for steady viscous flow in coiled circular pipes. *AIChE Journal*, 20(4):820-822. https://doi.org/10.1002/aic.690200427

Dean WR, 1927. XVI. Note on the motion of fluid in a curved pipe. *The London, Edinburgh, and Dublin Philosophical Magazine and Journal of Science*, 4(20):208-223. https://doi.org/10.1080/14786440708564324

Ferreira AR, Neves LA, Ribeiro JC, et al., 2015. Thiols' extraction from "jet-fuel" assisted by ionic liquids in hollow fibre membrane contactors. *Journal of Membrane Science*, 477:65-73. https://doi.org/10.1016/j.memsci.2014.11.057

Fuller EN, Schettler PD, Giddings JC, 1966. New method for prediction of binary gas-phase diffusion coefficients. *Industrial & Engineering Chemistry*, 58(5):18-27. https://doi.org/10.1021/ie50677a007

Henares M, Ferrero P, San-Valero P, et al., 2018. Performance of a polypropylene membrane contactor for the recovery of dissolved methane from anaerobic effluents: mass transfer evaluation, long-term operation and cleaning strategies. *Journal of Membrane Science*, 563:926-937. https://doi.org/10.1016/j.memsci.2018.06.045

Hitsov I, Maere T, de Sitter K, et al., 2015. Modelling approaches in membrane distillation: a critical review. *Separation and Purification Technology*, 142:48-64. https://doi.org/10.1016/j.seppur.2014.12.026

Jani JM, Wessling M, Lammertink RGH, 2011. Geometrical influence on mixing in helical porous membrane microcontactors. *Journal of Membrane Science*, 378(1-2):351-358. https://doi.org/10.1016/j.memsci.2011.05.021

Kaufhold D, Kopf F, Wolff C, et al., 2012. Generation of Dean vortices and enhancement of oxygen transfer rates in membrane contactors for different hollow fiber geometries. *Journal of Membrane Science*, 423-424:342-347. https://doi.org/10.1016/j.memsci.2012.08.035

Kong QR, Cheng YW, Bao XX, et al., 2013. Solubility and partition coefficient of *p*-toluic acid in *p*-xylene and water. *Fluid Phase Equilibria*, 340:46-51. https://doi.org/10.1016/j.fluid.2012.12.009

Kong QR, Cheng YW, Wang LJ, et al., 2016. Non-dispersive solvent extraction of *p*-toluic acid from purified terephthalic acid plant wastewater with *p*-xylene as extractant. *Journal of Zhejiang University-SCIENCE A (Applied Physics & Engineering)*, 17(10):828-840. https://doi.org/10.1631/jzus.A1500281

Kong QR, Cheng YW, Wang LJ, et al., 2017. Mass transfer enhancement in non-dispersive solvent extraction with helical hollow fiber enabling dean vortices. *AIChE Journal*, 63(8):3479-3490. https://doi.org/10.1002/aic.15700

Kong W, Zhu HY, Fei ZY, et al., 2012. A modified dusty gas model in the form of a Fick's model for the prediction of multicomponent mass transport in a solid oxide fuel cell anode. *Journal of Power Sources*, 206:171-178. https://doi.org/10.1016/j.jpowsour.2012.01.107

Lee J, Straub AP, Elimelech M, 2018. Vapor-gap membranes for highly selective osmotically driven desalination. *Journal of Membrane Science*, 555:407-417. https://doi.org/10.1016/j.memsci.2018.03.059

Li JF, Wang K, Zhang XB, et al., 2018. A parametric sensitivity study by numerical simulations on plume dispersion of the exhaust from a cryogenic wind tunnel. *Journal of Zhejiang University-SCIENCE A (Applied Physics & Engineering)*, 19(10):746-757. https://doi.org/10.1631/jzus.A1700632

Liu LY, Li LJ, Ding ZW, et al., 2005. Mass transfer enhancement in coiled hollow fiber membrane modules. *Journal of Membrane Science*, 264(1-2):113-121. https://doi.org/10.1016/j.memsci.2005.04.035

Mejia Mendez DL, Lemaitre C, Castel C, et al., 2017. Membrane contactors for process intensification of gas absorption into physical solvents: impact of Dean vortices. *Journal of Membrane Science*, 530:20-32. https://doi.org/10.1016/j.memsci.2017.02.016

Moll R, Veyret D, Charbit F, et al., 2007. Dean vortices applied to membrane process: Part I. Experimental approach. *Journal of Membrane Science*, 288(1-2):307-320. https://doi.org/10.1016/j.memsci.2006.11.030

Motevalian SP, Borhan A, Zhou HY, et al., 2016. Twisted hollow fiber membranes for enhanced mass transfer. *Journal of Membrane Science*, 514:586-594. https://doi.org/10.1016/j.memsci.2016.05.027

NIST (National Institute of Standards and Technology, US Department of Commerce), 2018. NIST Chemistry WebBook. USA. https://doi.org/10.18434/T4D303

Servi AT, Guillen-Burrieza E, Warsinger DM, et al., 2017. The effects of iCVD film thickness and conformality on the permeability and wetting of MD membranes. *Journal of Membrane Science*, 523:470-479. https://doi.org/10.1016/j.memsci.2016.10.008

Sethunga GSMDP, Rongwong W, Wang R, et al., 2018. Optimization of hydrophobic modification parameters of microporous polyvinylidene fluoride hollow-fiber membrane for biogas recovery from anaerobic membrane bioreactor effluent. *Journal of Membrane Science*, 548:510-518. https://doi.org/10.1016/j.memsci.2017.11.059

Shao JH, Liu HF, He YL, 2008. Boiler feed water deoxygenation using hollow fiber membrane contactor. *Desalination*, 234(1-3):370-377. https://doi.org/10.1016/j.desal.2007.09.106

Solsvik J, Jakobsen HA, 2011. Modeling of multicomponent mass diffusion in porous spherical pellets: application to steam methane reforming and methanol synthesis. *Chemical Engineering Science*, 66(9):1986-2000. https://doi.org/10.1016/j.ces.2011.01.060

Tan XY, Capar G, Li K, 2005. Analysis of dissolved oxygen removal in hollow fibre membrane modules: effect of

water vapour. *Journal of Membrane Science*, 251(1-2): 111-119. https://doi.org/10.1016/j.memsci.2004.11.005

Turri F, Yanagihara JI, 2011. Computer-assisted numerical analysis for oxygen and carbon dioxide mass transfer in blood oxygenators. *Artificial Organs*, 35(6):579-592. https://doi.org/10.1111/j.1525-1594.2010.01150.x

Wilke CR, 1950. A viscosity equation for gas mixtures. *The Journal of Chemical Physics*, 18(4):517-519. https://doi.org/10.1063/1.1747673

Wilke CR, Chang P, 1955. Correlation of diffusion coefficients in dilute solutions. *AIChE Journal*, 1(2):264-270. https://doi.org/10.1002/aic.690010222

Wu CR, Wang ZY, Liu SH, et al., 2018. Simultaneous permeability, selectivity and antibacterial property improvement of PVC ultrafiltration membranes via in-situ quaternization. *Journal of Membrane Science*, 548:50-58. https://doi.org/10.1016/j.memsci.2017.11.008

Wu DZ, Han Y, Zhao L, et al., 2018. Scale-up of zeolite-Y/polyethersulfone substrate for composite membrane fabrication in CO_2 separation. *Journal of Membrane Science*, 562:56-66. https://doi.org/10.1016/j.memsci.2018.05.021

Zhang JS, Zhang BZ, 2000. The third-order effect of curvature and torsion on the flow in helical circular pipe. *Acta Aerodynamica Sinica*, 18(3):288-299 (in Chinese). https://doi.org/10.3969/j.issn.0258-1825.2000.03.005

Zhou Y, Shah S, 2004. Fluid flow in coiled tubing: a literature review and experimental investigation. *Journal of Canadian Petroleum Technology*, 43(6), No. PETSOC-04-06-03 https://doi.org/10.2118/04-06-03

List of electronic supplementary materials

Fig. S1 Concentration profiles of N_2 of (a) HHFM deoxygenation (κ=162.9 m^{-1}, z=0.5 m), (b) SHFM deoxygenation (κ=0, z=0.5 m) on the cross-section and (c) HHFM deoxygenation (κ=162.9 m^{-1}), (d) SHFM deoxygenation (κ=0) along the axis direction. Re=217, T=298.2 K, $\bar{v}=0.5\,m/s$, p/p_0=0.50, and l=1.0 m.

Fig. S2 Porous membrane concentration profiles of H_2O vapor of (a) HHFM deoxygenation (κ=162.9 m^{-1}, z=0.5 m), (b) SHFM deoxygenation (κ=0, z=0.5 m) on the cross-section and (c) HHFM deoxygenation (κ=162.9 m^{-1}), (d) SHFM deoxygenation (κ=0) along the axis direction. Re=217, T=298.2 K, $\bar{v}=0.5\,m/s$, p/p_0=0.50, and l=1.0 m.

Table S1 Parameters used for simulation.

Table S2 Experimental data of HHFM and SHFM deoxygenation.

Table S3 Experimental results of long-time run for 100 h at Re=43.5, T=298.2 K, κ=162.9 m^{-1}, $\bar{v}=0.1\,m/s$, and p/p_0=0.50.

Table S4 Boundary conditions used to model Liu (2005)'s and Kaufhold (2012)'s work.

中文概要

题　目： 中空纤维膜脱氧过程中 Dean 涡强化传质研究

目　的： 在螺旋中空纤维膜脱氧过程中引入了 Dean 涡，与线型中空纤维膜脱氧过程相比传质速率显著提升。本文旨在建立新的螺旋中空纤维膜脱氧过程传质模型，探讨管程流体雷诺数、中空纤维膜结构参数、壳程真空度和操作温度对 Dean 涡强化传质效果的影响，并优化螺旋中空纤维膜脱氧过程操作参数。

创新点： 1. 建立新的螺旋中空纤维膜脱氧过程传质模型；2. 该传质模型可以应用于任何螺旋中空纤维膜气-液过程的传质行为描述。

方　法： 1. 实验研究管程流体雷诺数、中空纤维膜结构参数、壳程真空度和操作温度对 Dean 涡强化传质效果的影响，并与线型中空纤维膜传质进行对比。2. 利用螺旋坐标系下的质量连续性方程以及 Dean 涡的摄动解描述管程溶质的传质行为；利用改进的尘气模型描述膜孔道内多组份气体的扩散行为；耦合建立新的螺旋中空纤维膜脱氧过程传质模型，并与实验结果进行比较。3. 模拟脱氧过程的氧、氮、水三种组分的浓度分布，优化螺旋中空纤维膜脱氧过程的膜结构参数和操作参数。

结　论： 1. 实验和模拟结果均证实 Dean 涡可以有效提升脱氧传质速率，最大传质增强因子为 2.2。2. Dean 涡主要受到管程雷诺数和中空纤维膜曲率的影响；当管程雷诺数较大时，中空纤维膜即使存在很小的曲率，传质的速率也有显著的提升。

关键词： 传质；中空纤维膜；水脱氧；Dean 涡